NTNU – Trondheim
Norwegian University of
Science and Technology

Gold Nanostructures on Graphite

Erlend Espeland

Master of Science in Physics and Mathematics
Submission date: June 2013
Supervisor: Steinar Raaen, IFY
Co-supervisor: Armen Julukian, IFY

Norwegian University of Science and Technology
Department of Physics

Abstract

Gold nanoparticles supported on a graphite substrate are prepared by thermal evaporation, and subsequently studied by X-ray photoelectron spectroscopy (XPS), temperature programmed desorption (TPD) of carbon monoxide and scanning electron microscopy (SEM). Increasing the amount of gold deposited leads to a shift of the desorption peak to higher temperatures, and the gold particles become larger. Depositing approximately the same amount of gold at different evaporation ratios does not seem to affect the desorption. Triangularly shaped gold particles appeared at higher evaporation rates. This is thought to be caused by diffusion effects dominating the formation of the particles [1, 2].

Sammendrag

Nanopartikler av gull på et substrat av grafitt er blitt fremstilt ved hjelp av termisk pådampning, og deretter studert med fotoemisjonsspektroskopi (XPS), temperatur-programmert desorpsjon (TPD) av karbonmonoksid og sveipelektronmikroskopi (SEM). Økning i mengden gull som pådampes gir en forskyvning i desorpsjonstoppen mot høyere temperaturer og gjør at gullpartiklene blir større. Pådampning av omtrent den samme mengden gull ved forskjellige pådampningsrater virker ikke å ha noen påvirkning på desorpsjonen. Trekantformede gullpartikler dukker opp ved høyere pådampningsrater. Dette er trolig forårsaket av at diffusjonseffekter dominerer formasjonen av partiklene [1, 2].

Preface

This thesis is submitted as a required part of my Master of Science degree at the Norwegian University for Science and Technology in Trondheim.

I would like to thank my supervisor prof. Steinar Raaen and co-supervisor Armen Julukian for invaluable help in the lab and important feedback while writing this report. Assistance with the SEM imaging by Stefanus Lumban Tobing is greatly appreciated. Finally, I would like to thank my family and friends for all their support during my work with this thesis.

"Holy, holy, holy is the LORD Almighty
the whole earth is full of his glory."

– Isaiah 6:4

Trondheim
June 14, 2013

Erlend Espeland

Contents

Chapter 1

Introduction

Heterogeneous catalysis is an important part of many technologies, increasing yield and selectivity in both large and small scale chemical production. Nanoparticles of a catalytic metal supported on a substrate is a model for catalysts that can be conveniently studied. Compared to surfaces made from single crystals they contain new degrees of freedom that might influence the catalytic process, such as size and shape of particles, and the interface between the particles and the supporting substrate.

Earlier studies by *Julukian et. al.* [3] have indicated that the catalytic properties of platinum particles supported on graphite changes with particle size. Examining a similar system using gold rather than platinum is interesting, as gold is a widely used catalyst. *Karlsen* [4] deposited gold on a graphite substrate, but found no change in catalytic activity. There the sizes of the gold particles were much larger than for the platinum particles. By making supported gold particles of the same scale as the platinum particles, it can be examined whether the size has a similar effect on desorption for the gold particles as for platinum.

With this aim, gold nanoparticles are prepared by depositing small amounts of gold on to graphite substrates by thermal evaporation. The samples are then studied by X-ray photoelectron spectroscopy to get an indication of the amount of gold on the sample, and to look for shifts in core level binding energies associated with changes of particle size [1,3]. Temperature programmed desorption is performed to look for changes in the desorption of carbon monoxide that can be associated with particle shapes and sizes. The desorption properties of the system are interesting, as desorption is the last step of the heterogeneous catal-

ysis. Scanning electron microscopy is used to image some of the samples. These images are used to examine the size, shape and distribution of the nanoparticles.

Chapter 2

Theory

2.1 X-ray Photoelectron Spectroscopy (XPS)

Unless otherwise stated, this section is based on *Brundle et. al.* [5].

The working principle of XPS is simple. X-rays are radiated on to the surface that is to be analysed. By the mechanisms of the photoelectric effect, photoelectrons are ejected from the surface and move with a well defined kinetic energy (KE). Some of these are subsequently collected by an analyser which measures their kinetic energy. This is a very surface-sensitive technique, and is therefore useful for studying the structures at hand.

2.1.1 Basic principles

The electrons bound to an atom occupy discrete energy levels. The energy levels are grouped into shells labelled n, where $n = 1, 2, 3, \cdots$. The shells contain one or more subshells denoted *s, p, d, f, g,*$\cdots$. Because electrons obey the Pauli exclusion principle, only a limited number of electrons can occupy each shell. A schematic view of the shells with the lowest energy can be seen in figure 2.3. The shells fill in an order that minimizes the energy [6].

When an atom of the sample absorbs an X-ray photon, an electron from an atomic core level is ejected with a well defined KE given by

$$KE = h\nu - (BE + \phi). \tag{2.1}$$

Here h is the Planck constant, ν is the frequency of the X-ray radiation, KE is the kinetic energy, BE is the binding energy and ϕ is called the work function.

The work function ϕ is the difference between the Fermi level and the energy of the free electron, as seen in figure 2.3. The kinetic energies of the escaping electrons are measured by the analyser, and the work function is known [7, 8]. By eq. (2.1), BE can then easily be found as the only unknown variable. A plot of the number of counted electrons versus BE is an XPS-spectrum.

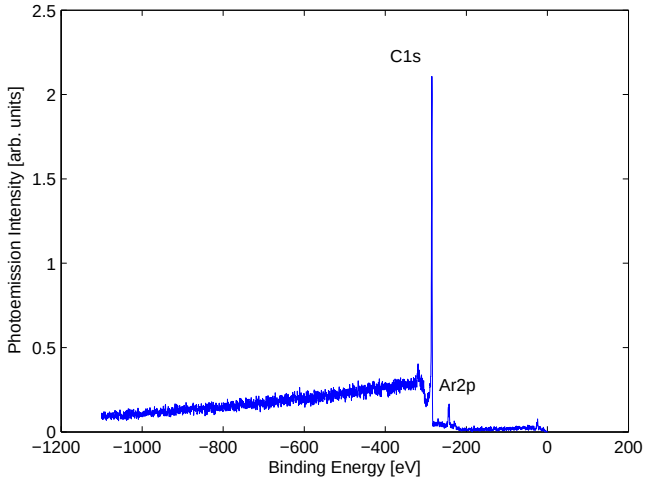

Figure 2.1: An XPS survey scan of graphite substrate. The main peaks are labelled. The Ar2p peak is caused by argon left on the sample after ion beam sputtering was used to clean it.

The main peaks that can be seen in fig. 2.1 are formed by the electrons that escape without loosing energy. The energy of these peaks correspond to the BE of the core level electrons in the atoms. They are characteristic of the elements present in the sample, and can be used as a fingerprint to identify the elements present.

Electrons that suffer energy losses reach the analyser with a lower KE than the electrons that do not suffer losses, and are interpreted as having a higher BE. These electrons contribute to a significant background signal. Electrons that suffer energy losses by continuous energy processes, like inelastic scattering, form a continuous "tail" behind the main peak that is formed by the lossless electrons. A "tail" of this kind can be seen to the left of the C1s peak in figure

2.1. If the electrons lose energy due to a discrete processes, like i.e. plasmon excitations, they will form a small subpeak [9].

The average length an electron can travel in a solid without suffering inelastic losses is called the *mean free path*. Figure 2.2 shows the mean free path for various electron energies in some elements. In XPS we deal with electrons with KE in the range 5 eV to 2000 eV. They have a mean free path in the range of about 4 Å to 40 Å. This means that XPS is a very surface-sensitive technique [9].

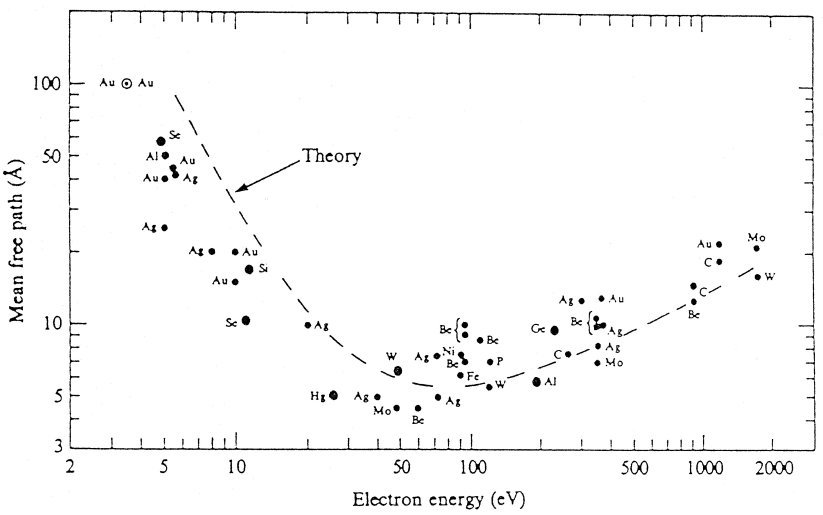

Figure 2.2: Mean free path for electrons in solids as a function of kinetic energy for various elements. Theoretical predictions are shown as dotted line [10].

The decay of the core hole left by an emitted electron can cause either a photon or an additional electron to be emitted, with a certain probability. When an electron is emitted in this way, it is called an Auger process. The emitted Auger electron has a KE that is only dependent on the energy levels of the core hole, the decaying electron, and the work function. Auger electrons will show up as Auger peaks in the XPS spectrum, and can be used to identify elements present in the sample. They are however relatively weak compared to the photoelectron peaks.

The interaction between the electronic orbital angular momentum and electron spin causes an energy difference between spin up and spin down electrons

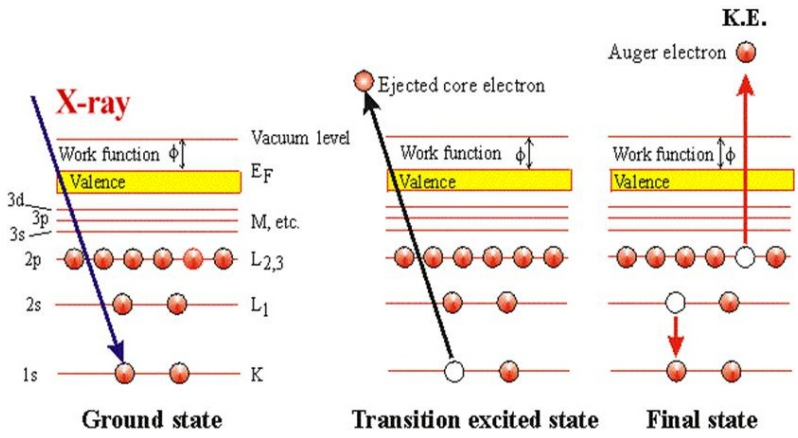

Figure 2.3: Schematic view of photoelectron emission processes. In XPS, the electrons measured are ejected directly from core levels. Auger Electron Spectroscopy, in contrast, measures Auger electrons that can be ejected as core level holes are filled [11].

in partly occupied orbitals. This causes the signal from orbitals to be split into doublet peaks, and is called spin-orbit splitting. The s orbitals are not spin-orbit split, as they they are spherical and thus have no orbital angular momentum.

The cross-section for photoelectric interaction varies between different orbitals, elements and spin-orbit couplings. This leads to a relative difference in peak intensity between different peaks for the same incoming intensity of X-rays. Using this, one can calculate an intensity for each peak that is comparable to other peaks. This intensity is given by

$$I = \frac{A}{SF \cdot n \cdot s} \tag{2.2}$$

where A is the area of the peak after subtracting the background signal, SF is the sensitivity factor, n is the number of iterations and s is the relative number of electrons in a peak with spin-orbit splitting if only one peak of the doublet is taken into account. The sensitivity factor is a measurement of the reaction cross-section, and is tabulated for the relevant peaks [12].

Using the intensity calculated with eq. (2.2) it is possible to make an approximation of the thickness of a thin film on a substrate. A sketch of such a system is shown in figure 2.4. Using a crude continuum model, where the photoemission electrons from lower layers in the surface are exponentially attenuated by the layers above we find, using the intensities found by (2.2):

$$I_{sub} = \int_a^\infty e^{-\frac{x}{\lambda}} dx = \lambda e^{\frac{a}{\lambda}} \tag{2.3}$$

$$I_{film} = \int_0^a e^{-\frac{x}{\lambda}} dx = \lambda(1 - e^{\frac{a}{\lambda}}) \tag{2.4}$$

$$\frac{I_{film}}{I_{sub}} = \frac{\lambda(1 - e^{\frac{a}{\lambda}})}{\lambda e^{\frac{a}{\lambda}}} = e^{\frac{a}{\lambda}} - 1 \tag{2.5}$$

$$e^{\frac{a}{\lambda}} = \frac{I_{film}}{I_{sub}} + 1 \tag{2.6}$$

$$a = \lambda \ln(\frac{I_{film}}{I_{sub}} + 1) \tag{2.7}$$

Here I_{sub} and I_{film} are the photoemission intensities from the substrate and film respectively, a is the approximate thickness of the film, and λ is the electron mean free path.

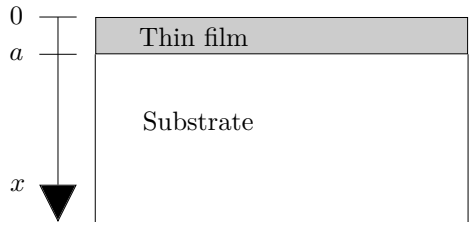

Figure 2.4: Schematic view of thin film on substrate.

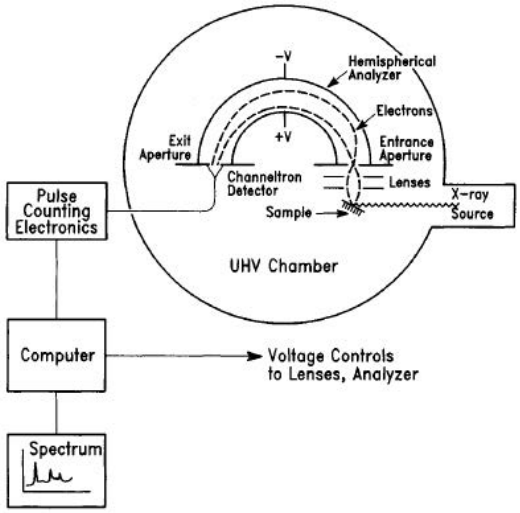

Figure 2.5: Schematic view of the instrumentation used for XPS [5].

2.1.2 Instrumentation

Figure 2.5 shows a schematic view of an XPS-system. The X-ray source consists of an Al anode that is bombarded by electrons accelerated by a high voltage supply. The main Al X-ray radiation line, called $K\alpha$, has photons with energy 1486.6 eV. A monochromator made from single crystal silicon focuses the

beam onto a smaller, but still macroscopic, area of the sample. It also scatters away satellite radiation lines, and sharpens the width of the main line to (1486.6 ± 0.5) eV, which gives a better resolution. After leaving the sample, some of the electrons are slowed down and focused into the analyser by a series of electromagnetic lenses. Slower electrons are easier to measure. The analyser consists of two concentric hemispheres with a voltage applied across them. The voltage across the analyser is usually fixed, and the voltages of the lenses varied. The combination of voltages across the lenses and the analyser focuses the trajectories of electrons of a certain KE range on a detector. Electrons with other energies do not reach the detector. This makes it possible to scan the spectrum of energies up to $KE < h\nu$. In modern XPS instrumentation, an area detector is usually used to detect electrons within a range of energies simultaneously. The relevant work function to use in eq. (2.1) is the work function of the analyser. Analysers are usually calibrated with reference to a standard photoelectron line [7, 8]. This way the BE peaks remain stationary even though the samples are changed. Computer software is used for control of the instrumentation, and analysis. To avoid overheating, the X-ray source is water-cooled.

2.2 Temperature Programmed Desorption (TPD)

TPD is an experimental technique used to examine the thermodynamic properties of adsorption systems. Heterogeneous catalysis on surfaces is very important in industrial chemical processes, increasing both yield and purity of the products. Because desorption is the last step in such a catalytic process, desorption properties of surfaces are particularly interesting.

An equation called the *Arrhenius expression* is usually used to interpret TPD data. Based on this it can be shown that the desorption rate is given by

$$r_d = -\frac{dN}{dt} \propto \frac{d(\Delta P)}{dt} + \frac{\Delta P}{\tau}. \tag{2.8}$$

Here r_d is the desorption rate, N is the number of adsorbed particles, P is the partial pressure of some gas and τ is the pumping time. Eq. (2.8) shows that given a sufficiently small pumping time τ, the desorption rate is proportional to the change in the partial pressure [13].

In a TPD experiment a surface with some adsorbed molecules is heated at a constant rate, and the partial pressures of relevant gases close to the surface are

measured. The most important piece of equipment for doing TPD is the mass spectrometer used for measuring these partial pressures.

2.2.1 Quadropole Mass Spectrometer

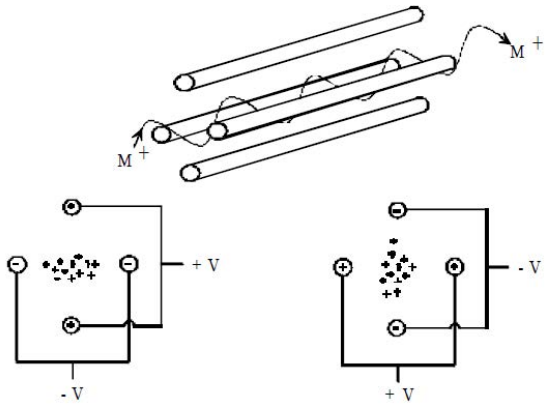

Figure 2.6: Top: Schematic view of the mass analyser in a Quadropole Mass Spectrometer. Top image shows the ion path through the quadropole electrodes. The bottom images shows how the ions are squeezed during the two halves of the analyser cycle [14].

Quadropole mass spectrometers (QMS) are the most common mass analysers. They can measure m/z ratios[1] up to the range of 500, or even as much as 4000 for some models.

As shown in figure 2.6, the analyser consists of four rod-shaped electrodes. The gas that will be analysed is first ionized, then accelerated into the space between the electrodes. A radiofrequency AC voltage is applied across a pair of electrodes, alternating between the two pairs. A DC voltage is superimposed on this. The effect of these fields is to make the ions of the gas move in a three-dimensional wave pattern as they travel trough the analyser. The ions with higher m/z ratio accelerated less by the alternating field than those with low m/z ratio. They are however accelerated more by the DC field. By tuning

[1]Here m is the mass of the ion given in atomic mass units, and z is the charge given in unit charges

the frequencies and voltages, it is possible to make high and low pass filters for ions based on their m/z ratio. A detector at the end of the QMS detects the flux of ions at each m/z ratio [14].

2.3 Scanning Electron Microscopy (SEM)

This section is based on *Mills et. al.* [15] and *Dunlap et. al.* [16].

In scanning electron microscopy (SEM) an electron beam is raster scanned over a surface, and the resulting signals are used to examine the properties of the sample. This is a powerful technique, especially for examining the topography and composition of samples. A very broad range of magnification facilitates the correlation between properties on a macro, micro and nano scale. Using electrons instead of light photons to illuminate the sample increases the resolution. A high depth of field eases identification of sample features. SEM can also be used to characterize the elemental composition of a sample by analysing backscattered electrons and characteristic X-rays emitted. Figure 2.7 shows a schematic view of the SEM instrumentation.

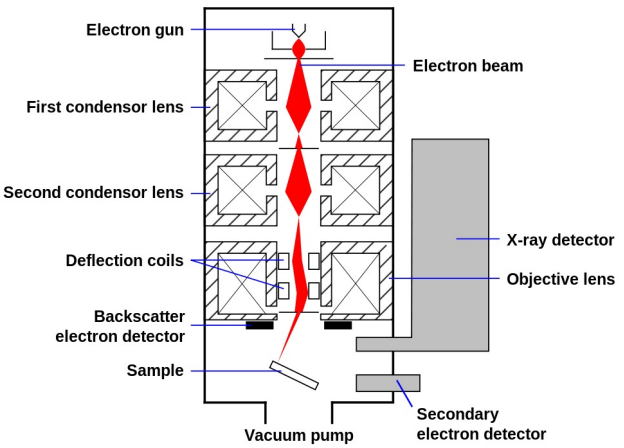

Figure 2.7: Schematic view of SEM instrumentation [17].

A scanning electron microscope has four main parts. The illumination system creates an electron beam that is focused on to the sample using a series of

apertures and electromagnetic lenses. The information system consists of the signals created by the interaction of the beam with the sample, and the detectors for these signals. The display system displays this information on some kind of screen or photographic medium. Lastly, a vacuum system is needed to remove gases that would otherwise interfere with the system. Vacuum systems are discussed in section 2.4.

The electron beam is created at the top of the column using an electron gun. Electromagnetic lenses in combination with apertures are used to control the intensity and size of the electron beam, and focus it on to the sample. Deflection coils are used to deflect the beam in the x- and y-directions so that the beam can be scanned over the area that will be imaged. The information recorded at each point the beam is positioned during this scan is composited into the final image.

Several signals are created when the electron beam interacts with the sample, depending on how the electrons interact with the sample material. Electrons will be scattered, either elastically by interaction with nuclei or inelastically by interaction with electrons in the sample material. Other signals are characteristic X-rays, phonons, light from cathodoluminescence, sample current and transmitted electrons. These signals can then be recorded using various sensors inside the sample chamber.

It is mostly the secondary electrons that are used for actually imaging the sample. These have relatively low energies (less than 50 eV). Because of this, most of the secondary electrons that escape the sample will originate close to the surface. Electrons from the primary beam will interact with the sample in a limited volume that is dependent on the sample material and the energy of the primary beam electrons. The intersection between this volume and the sample surface will be dependent on the topography locally on the sample. This is illustrated in figure 2.8. Changes in the number of electrons detected caused by this gives the contrast in the image. To increase the signal strength, the sample is often tilted towards the detector so more of the electrons emitted can be collected. Some types of secondary electrons, such as those originating from the detector itself, are unwanted noise and will be filtered out prior to detection. Although there are several types of detectors for secondary electrons in use, the in-lens type is most common as it gives clearer images [4].

Electrons that are inelastically backscattered from the sample carry compositional information because the probability for backscattering depends on the atomic number of the element the electron interacts with. The number of backscattered electrons detected can be used to distinguish between different elements. Together with analysis of characteristic X-rays emitted by the sample

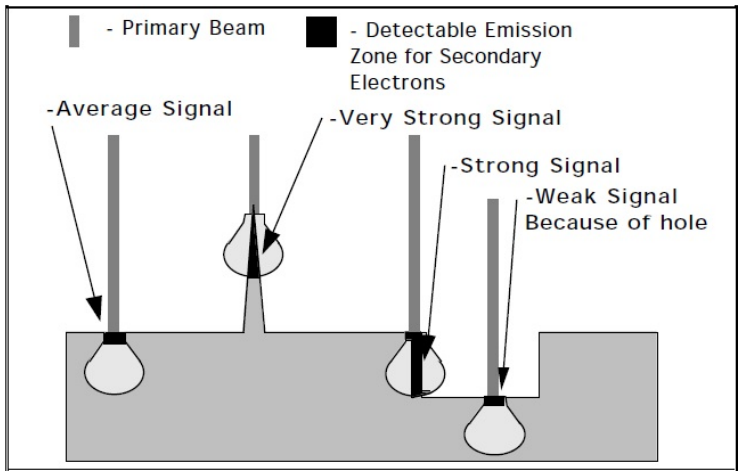

Figure 2.8: The topography of the sample greatly influence the signal strength for secondary electron emission when using SEM. The lightly shaded areas indicate the volume where the primary electron beam interacts with the sample material. The figure illustrates how the surface area of the sample that is within this volume is highly dependent on the topography of the sample. Only secondary electrons released near this surface will escape the sample and contribute to the signal [16].

this can be a powerful technique for analysing the composition of the sample. Various other type of signals, like i.e. light from cathodoluminescence, can also be used to examine the properties of the sample.

2.4 Ultra High Vacuum

Unless otherwise stated, this section is based on *Moore et. al.* [18].

An ultra high vacuum (UHV) is defined as a diluted gas with a pressure below 10^{-7} mbar, while it is called high vacuum when the pressure is between 10^{-3} and 10^{-7} mbar. In the UHV-regime, the dimensions of the apparatus ($\sim$1 m) are far smaller than the mean free path of the gas particles ($\sim 10^4$ m). When doing surface science experiments, UHV is needed to keep surfaces clean and avoid contamination during the experiment. High vacuum is also needed to avoid scattering of the electrons in transit when doing surface electron spectroscopy.

2.4.1 Turbomolecular pump

A turbomolecular ("turbo") pump consists of a series of turbine blades. These are alternately rotating and stationary. The the rotating blades have a typical speed in the range of 50 000 rpm.

The gas molecules that enter the pump collide with the rotating blades. These are canted toward the exit, so that the molecules are given an added momentum in this direction. Several such collisions will transport the molecule to the pump outlet. The turbo pump needs a low pressure at the outlet to function. This is achieved by using a low vacuum pump as a forepump.

2.4.2 Ion pump

Ion pumps mainly consist of a stainless steel anode and a titanium cathode with a high voltage across, usually around 7 kV. Gas molecules that enter the volume between them are ionized, and then accelerated towards the anode. There they are captured, either by chemisorption or by being buried deep in the cathode. Ion pumps are particularly good at pumping light and inert species.

Chapter 3

Experimental

3.1 Experimental column

The apparatus used in this experiment consists of four vacuum chambers housing the rest of the equipment used. A picture of the experimental column is shown in figure 3.1. The main vacuum chambers and the mass spectrometer are highlighted. The two main chambers are able to reach pressures in the low 10^{-10} torr[1] range.

3.1.1 Loading dock

The loading dock is where samples are inserted into and removed from the vacuum system. It also houses the manipulator arm used to insert the samples into the main vertical manipulator arm in the preparation chamber. Area A in figure 3.1 shows the loading dock.

While samples are being inserted or removed, the loading dock is exposed to atmosphere for as short time as possible to avoid contaminating the chamber. Care is also taken to avoid contaminating the parts on the inside of the chamber when inserting and extracting samples. The vacuum in the loading dock is maintained by a small turbopump. After inserting a sample, the valve to the preparation chamber should not be opened until the pressure is below

[1] Torr is a non-SI unit for pressure commonly used in experimental set-ups. It is defined by 1 torr = 1/760 atm, and 1 torr = 1.333 mbar

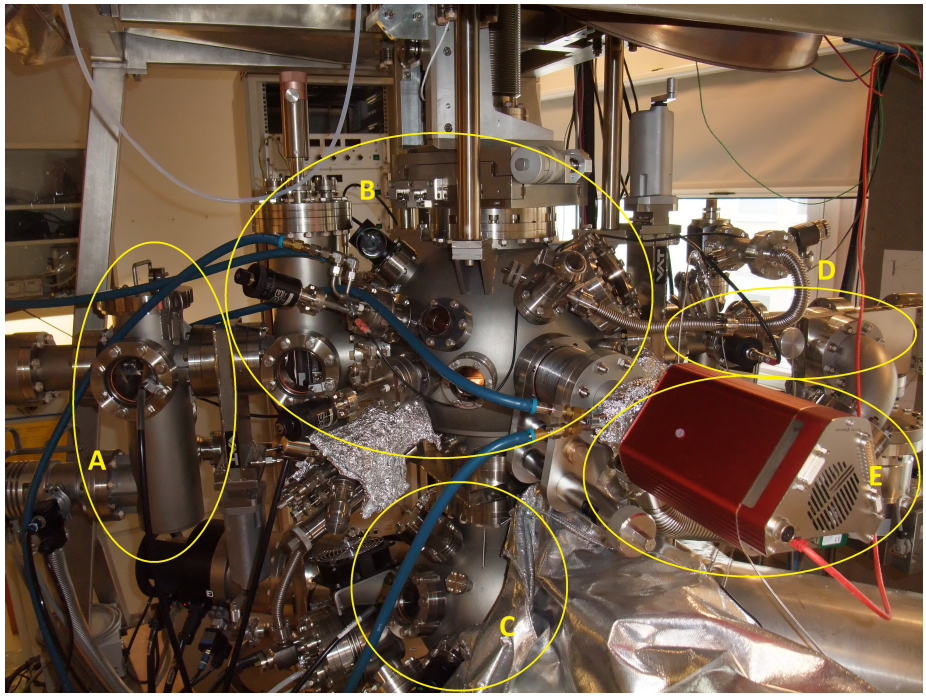

Figure 3.1: Apparatus used for the experiments described in this report. A: Loading dock, also housing manipulator arm. B: Preparation chamber, housing evaporation source, sputtering source and mass spectrometer. C: Analysis chamber, housing XPS system. D: Reaction chamber, not used for these experiments. E: Quadropole mass spectrometer.

10^{-7} mbar. This is to avoid degrading the conditions for vacuum in the preparation chamber.

3.1.2 Preparation chamber

The preparation chamber is where the sample is loaded on to the vertical manipulator arm. It houses a magazine that can store up to six samples so they do not need to be removed from vacuum. This is also where the evaporator and the mass spectrometer is located. The vacuum is maintained by a dedicated

turbopump. Area B in figure 3.1 shows the preparation chamber.

The vertical manipulator arm is used to position the sample appropriately in the column for the various operations. It is moved up and down by a computer controlled motor, and the angle and pitch is adjusted manually. The manipulator has electrical connectors for the heating and thermocouple on the sample holder. It also houses the pipes used to transport liquid nitrogen to cool the sample. Degassing of the samples is done in this chamber while it is closed off from all the other chambers.

3.1.3 Analysis chamber

The analysis chamber houses the systems used for XPS measurements, including an Al K_α x-ray source (Scienta), the monochormator and the analyser (Scienta SES2002). It is shown in area C of figure 3.1.

The pressure is maintained by a turbo pump and an ion pump. The turbopump exhausts into the same low vacuum pump as the preparation chamber pump. This can lead to pressure leaks between the chambers. Because of this the valve to the turbopump in the analysis chamber is always closed when the chamber is not in use. To maintain UHV in the analysis chamber, the valve to the preparation chamber is not opened unless the pressure in the preparation chamber is below 10^{-9} torr.

3.1.4 Reaction chamber and differentially pumped mass spectrometer

The reaction chamber is shown in area D of figure 3.1. It is used if there is need for a sample to be exposed to gases at relatively high pressures, up to atmospheric pressure.

Area E shows the mass spectrometer (Pfeiffer vacuum - PrismaPlus). It has an inlet constrained by a nozzle inside the preparation chamber. The mass spectrometer is also connected to the reaction chamber, to enable the turbo pump connected there to pump gas molecules from the tip of the nozzle through to the pump. This set-up is why this is called a differentially pumped mass spectrometer. Because the mass spectrometer can measure any gas molecules that arrive at the analyser, even through normal dispersion in the chamber, this should increase the sensitivity to gases present at surfaces close to the tip of the nozzle compared to a system that is not differentially pumped.

3.2 Sample preparation

The nine samples used for the experiments are made from graphite film. The film has a thickness of 0.2 mm and a purity of 99.8 %. It was obtained from Goodfellow Cambridge Ltd. Samples are cut from the sheet of graphite film using scissors or a scalpel to get pieces of the desired size.

The samples need to be mounted in holders specially designed for use in the UHV camber. To avoid contaminating the samples or the holders, gloves are worn at all times when handling them.

Two different sample holders were used in the experiments. They can be seen in figure 3.2. The holders are two different models based on the same basic design, labelled respectively holder A and holder B. They have lips that fit into the grooves in the vacuum chamber that are designed to fix the sample holders in place. One larger and one smaller lip ensures that the sample holders are always inserted the right way. The screws seen on the back of the holders double as contacts. Two are for the thermocouple, two are for the heating filament, and two are for grounding the sample and holder. Sample holder B does not have dedicated contacts for grounding, but the sample is still grounded through the thermocouple. Table 3.1 lists what sample holder was used for the various samples.

3.2.1 Sample mounting

All the samples were mounted in one of the sample holders shown in figure 3.2. Table 3.1 shows which sample holder was used for each sample. For sample holder A, the thermocouple is pressed underneath the sample, and the mask is fastened on top in order to keep the sample in place. On sample holder B, the thermocouple is fastened with a screw directly on to the same metal plate that the sample is mounted on. Because this metal plate has very good thermal conductivity, it is assumed that it has the same temperature at the positions of both the sample and the thermocouple. The sample is heated by passing a current through a heating filament that is isolated from the sample by a ceramic disc.

During the experiments, the sample holders have been somewhat unstable. Their performance has deteriorated after being only a few uses. In particular, the heating filament tend to partially short circuit, leading to unstable heating of the sample. Regular and time consuming maintenance had to be performed on the sample holders to keep their performance within acceptable limits.

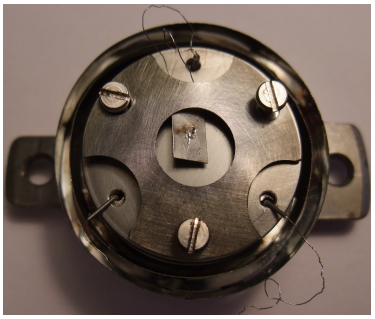

(a) Front of sample holder A.

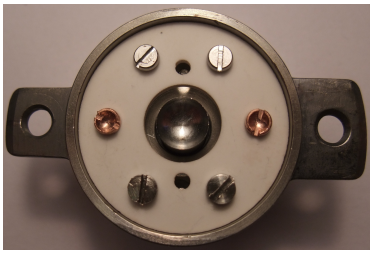

(b) Back of sample holder A.

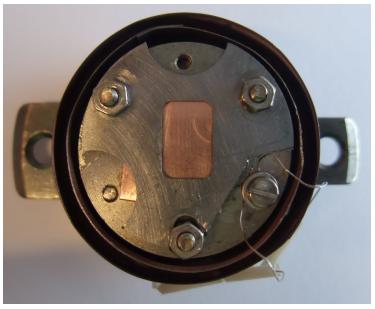

(c) Front of sample holder B.

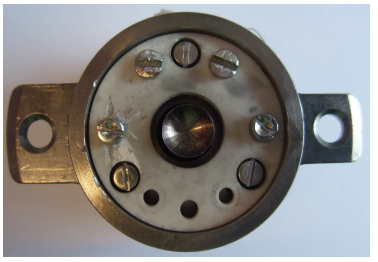

(d) Back of sample holder B.

Figure 3.2: Sample holders of the type two types used in the experiments, labelled type A and type B. (a): The front of the sample holder A. The thermocouple can be seen through the hole in the mask that is used to hold the sample in place. The two other wires are for grounding the sample. (b): The back of sample holder A. The six screws double as electrical contacts. The middle two are for the heating filament, while the other four are contacts for the thermocouple and for grounding the sample. (c): The front of sample holder B. Seen through the mask is the copper plate the sample rests on. On this model the thermocouple is fastened by a screw on the lower left side of the holder. (d): The back of sample holder B. The screws serve the same function as for sample holder A, although there are no contacts for grounding on this sample holder. The sample will still be grounded through the thermocouple.

3.2.2 Degassing

All the samples had to be degassed after insertion into the vacuum chamber to desorb any gases on the surface. This is done by alternately heating the samples and letting them cool, until the UHV was maintained at a temperature of 950 K. A proportional–integral–derivative (PID) controller[2] was used to control the temperature when degassing, and also when temperature control was needed at other times during the experiment.

3.2.3 Evaporation

Small amounts of gold are deposited on the graphite substrate. As the gold interacts weakly with the graphite substrate, the gold will aggregate and under the right conditions self assemble into nanostructures.

A small gold nugget rests in a basket shaped coil of tungsten wires. When current is passed through the wires, the nugget is heated and gold atoms evaporate. Because of the low pressure, they follow a line-of-sight trajectory to any surface, including the sample that is faced toward the evaporator.

The amount of gold deposited is controlled by varying the duration and intensity of the current through the heating filament. Using material from the nugget changes its surface area. Because of this, different heating currents and evaporation times may be needed at different times to deposit approximately the same amount of gold. It is important to note that the gold in the evaporator will be used up after extensive use, and a new gold nugget has to be inserted. The evaporator used was replaced between the evaporation of sample 3 and 4. Because of this, the evaporation currents used before and after this time are not directly comparable.

To get similar conditions for deposition, the samples were heated to 950 K at least once immediately prior to evaporation, and subsequently cooled to 310 K before evaporation. This temperature was maintained for the whole evaporation time. The heating current and evaporation times used can be seen in table 3.1. When evaporating, the evaporator was preheated for 40 s at the same current used for evaporation, but with the shutter closed. These 40 s are not included in the evaporation times listed in table 3.1, as it is assumed that no gold is deposited during this time.

Deposition of gold on sample 4 was done in two discrete steps. This is because the evaporator was replaced immediately prior to depositing gold on

[2]The controller is implemented by a LabView program made by Steinar Thorshaug for his project work in 2004.

this sample, and the current chosen at first led to too low amounts of gold being deposited on the sample. Sample 4 is therefore not directly comparable to the other samples. It is included in table 3.1 for completeness.

Earlier experiments have been carried out by the author where gold was deposited on highly oriented porylitic graphite [19]. Some of the gold was subsequently removed by ion beam sputtering. No gold structures were found on these samples when they were examined by SEM. It is likely that there were no gold left on the samples due to small amounts deposited and the subsequent sputtering. For this reason results from these samples are not included in this thesis.

Table 3.1: Evaporation current, evaporation time and sample holder used for the samples.

Sample	Current (A)	Time (s)	Sample holder
1	6.0	240	A
2	6.25	600	B
3	6.25	1200	A
4	6.5 and 7.25	60 and 60	B
5	7.25	180	A
6	7.75	90	B
7	8.25	55	B
8	8.75	60	B
9	9.25	30	B

3.3 Measurement

After the samples had been degassed as described above, an XPS survey scan was conducted to check that the surface was clean. If the scan confirmed that the substrate was clean, gold was deposited by evaporation according to table 3.1.

3.3.1 XPS measurements

XPS was performed with an acceleration voltage of 13 kV. The filament current was set so that the discharge current always was 19.1 mA. Using the same discharge current in all experiments ensures that the intensity of various XPS

measurements are directly comparable. The X-ray chamber was kept at a constant temperature of 328 K by a heating element.

After the XPS survey scan confirmed that the sample was not contaminated, the gold was deposited. An XPS measurement of the main peaks of the gold (Au4f) and of the carbon substrate (C1s) was executed. Table 3.2 lists the settings used when recording these spectra.

Table 3.2: Settings used for recording the XPS spectra of the three regions used.

Name	BE range (eV)	Number of iterations	Pass energy (eV)
Sweep	0 - 1100	2	500
C_1s	280 - 295	5	500
Au_4f	57 - 95	20	200

The XPS spectra were used both to look for shifts in the binding energy of gold, and to estimate the amount of gold on the sample. This estimation is done using the intensities calculated according to eq. (2.2). The ratio between the intensity of gold and carbon is used as a measure of the amount of gold on the sample. A MATLAB script was used to subtract the background signal and calculate the area under each peak. The sensitivity factors used are 1 for C1s and 17.66 for Au4f [12]. Figures 4.1 and 4.2 show examples of spectra of respectively C1s and Au4f. All spectra looked similar to this.

3.3.2 TPD measurements

TPD measurements were performed using carbon monoxide (CO) as the adsorbate gas. Because CO desorbs at low temperatures, the samples were cooled with liquid nitrogen while the TPD measurements were performed. How effectively this cooled the sample varied between the different sample holders and samples, but the lowest temperatures achieved were in the 95 K to 110 K range. To minimise the opportunity for contamination of the sample from gases present in the vacuum chamber, deposition and TPD were carried out the same day. Heating the samples to more than 450 K was avoided after gold had been deposited to make sure the surface structures were undisturbed.

The sample was kept at a temperature of 130 K while being dosed with CO. CO was introduced into the preparation chamber through a leak valve. The pressure in the chamber was held at $1 \cdot 10^{-8}$ torr for 10 minutes, equalling a

dose of 6 L[3]. It is assumed that this is well above the saturation dosage. After dosing, the sample was allowed to cool in order to reach a temperature suited for starting the TPD.

Due to degradation in the performance of the sample holders, different currents had to be used to get an approximately equal heating rate for the different samples when performing TPD. To find the appropriate heating current that should be used, a process of trial and error was used. Before the sample was dosed with CO, it was heated several times using different heating currents until a current giving an appropriate heating rate was found. Dosing was then carried out, before the mass spectrometer was positioned with the nozzle at the center of the sample, as close to the sample as possible while it could still be seen that it did not touch the sample surface. The sample was then heated using the constant current found to be appropriate during the trial heating, to get a smooth and approximately linear temperature increase. Partial pressures in the mass spectrometer and the temperature of the sample were recorded. For all samples, the TPD spectrum was recorded for the temperature range 105 K to 400 K. Table 3.3 shows the heating currents used, and the average heating rate between 110 K and 210 K for the various TPD measurements

Table 3.3: Heating currents used for recording TPD spectra, and the resulting heating rates. The listed rate is the average heating rate in the 110 K *to* 210 K *range, where most of the CO is desorbed.*

Sample	Heating current (A)	Average heating 110 K to 210 K (K/s)
1	6.0	1.59
2	6.6	1.54
3	7.0	1.59
4	6.6	1.21
5	7.0	1.68
6	6.0	1.64
7	6.0	1.41
8	6.0	1.47
9	6.8	1.67

The TPD was used to see how different evaporation rates or amounts of gold on the sample influenced the desorption of CO from the sample.

[3]The Langmuir, symbol L, is a unit of gas dosage to a surface. Exposure to a gas pressure of $1 \cdot 10^{-6}$ torr for 1 s equals a dosage of 1 L.

3.3.3 SEM measurements

Each sample was removed from the vacuum chamber and stored after the XPS and TPD measurements had been carried out. After all the samples had been prepared, some were selected for imaging by SEM based on the results from the XPS and TPD. Samples 1, 3, 6, 7 and 9 were chosen because they were though to be most likely to compliment the results obtained from the XPS and TPD measurements. Sample 7 did not give usable images. The number of samples imaged was limited by the time the SEM was available. A Zeiss Ultra FE (Field Emission) SEM was used for imaging.

Chapter 4

Results

The results of the XPS measurements are presented in section 4.1, while the results of the TPD are grouped in two different sections. Section 4.2 concerns the results found when examining the effect of the amount of gold deposited. This includes samples 1–3. Section 4.3 presents the results found when examining the effect of the evaporation rate. This includes samples 1, 5–7 and 9. Sample 4 is not included because evaporation was done in two separate stages for this sample, see section 3.2. Sample 8 is excluded because electronic noise destroyed the TPD data while it was being recorded.

4.1 XPS measurements

XPS spectra of sample 1 recorded after evaporation of gold on to the sample are shown in figures 4.1 and 4.2 for the C1s and Au4f peaks respectively. The XPS spectra recorded for the other samples were similar. They were used to calculate the photoemission intensity ratio of gold to carbon I_{Au}/I_C according to eq. (2.2). For the Au4f spectrum it should be noted that the peak is a doublet due to spin-orbit splitting of the electron energy levels, and that the rightmost peak was used for intensity calculations.

Table 4.1 lists the measured intensity ratios, the binding energy of the Au4f XPS peak and approximate TPD peak temperature for all the samples. When sample 4 was prepared evaporation was done in two separate stages on the same sample. The data is included for completeness, but will not be used in the following considerations.

Table 4.1: Table of intensity ratio, binding energy of the Au4f XPS peak and approximate TPD peak temperature for the samples used. For the binding energy the rightmost peak of the doublet is used, see figure 4.2. The TPD peak temperature is omitted for sample 8 because of noise on the TPD spectrum.

Sample	Intensity ratio	Au4f peak energy(eV)	TPD peak temperature (K)
1	0.0094	−84.38	123
2	0.049	−84.92	138
3	0.109	−84.38	141
4	0.0048	−84.38	154
5	0.0097	−84.38	139
6	0.0096	−84.47	143
7	0.0088	−84.56	142
8	0.0127	−84.56	–
9	0.0107	−84.47	140

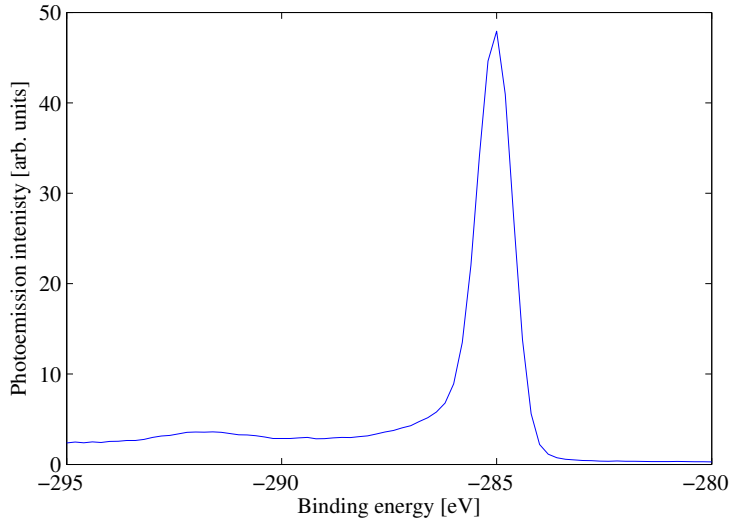

Figure 4.1: XPS spectrum of sample 1 after evaporation showing the C1s peak. All the C1s spectra recorded were similar to this. These spectra were used to calculate the intensity of carbon in the spectrum using eq. (2.2).

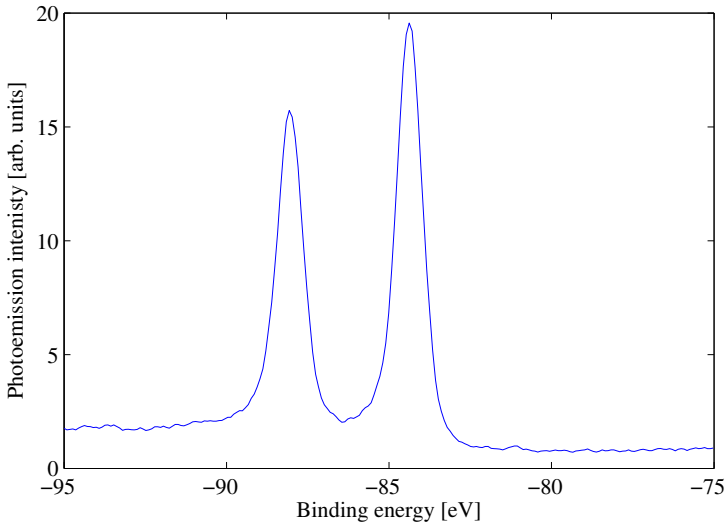

Figure 4.2: XPS spectrum from sample 1 after evaporation showing the Au4f doublet peaks. All the Au4f spectra recorded were similar to this. These spectra were used to calculate the intensity of gold in the spectrum using eq. (2.2). The peak is a doublet due to spin-orbit splitting. The rightmost peak was used for intensity calculations.

A small shift in the binding energy of the gold peaks were found for some of the samples when doing XPS measurements, but no trend was found in these shifts.

4.2 The effect of changing intensity ratio

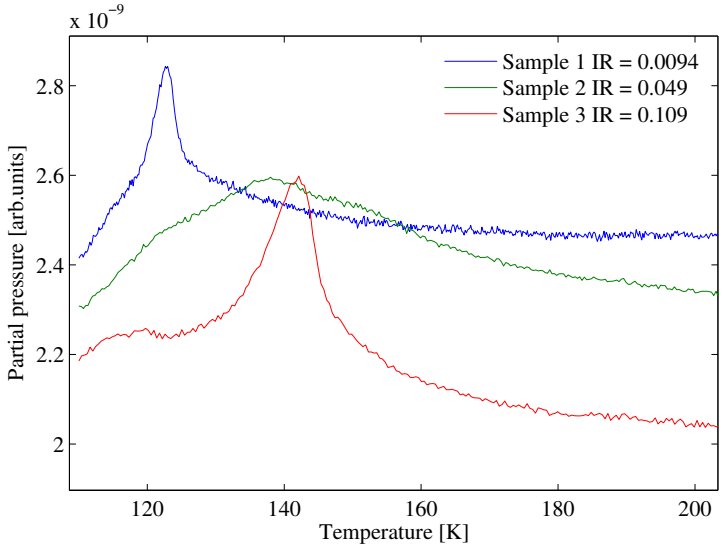

Figure 4.3: TPD spectra of samples 1–3. The intensity ratio of gold to carbon I_{Au}/I_C is given in the legend, calculated using eq. (2.2). Approximate peak temperatures can be found in table 4.1. A clear shift towards higher temperatures at the desorption peak can be seen for samples 2 and 3, which have higher intensity ratios. This shift is in total 18 K *from sample 1 to sample 3. Samples 1 and 3 have sharper peaks than sample 2. For sample 2 a shoulder can be seen around* 120 K. *Sample 3 has two peaks, one small at* 120 K *in addition to the main peak. Note that these spectra should also be compared to those shown in figure 4.6.*

Samples 1–3 are used to examine the effect of changing the amount of gold deposited. This amount is indicated by the intensity ratio I_{Au}/I_C, calculated

according to eq. 2.2. As can be seen in table 4.1, the intensity ratio for samples 2 and 3 are approximately 5 and 10 times as large as for sample 1 respectively. It should also be noted that samples 5–9 have similar intensity ratios as sample 1.

In figure 4.3 the TPD spectra from sample 1–3 for temperatures up to 200 K are shown. Although the spectra were recorded up to 400 K, they are truncated at 200 K because they are featureless above this temperature. A shift of the desorption peak of 18 K from sample 1 to sample 3 can be seen. Sample 2 has a broader and less well defined peak than samples 1 and 3, and the shift of this peak compared to the other samples is harder to determine. However, it seems that it is shifted about 15 K from sample 1. It should be noted that the relative increase in intensity ratio from sample 1 to 2 is much larger than from sample 2 to 3.

There are some other features in the TPD spectra that also should be noted. In the spectrum from sample 2 a feature where the partial pressure rate of change slows down (a shoulder) can be seen around 120 K. Sample 3 has a small peak located in the same area. This is the only spectrum with a clearly identifiable second peak, but this peak is significantly smaller and less distinct than the main peak.

A SEM image from sample 1 is shown in figure 4.4. Gold particles can be seen as bright dots in the image. These are unevenly distributed. Some areas have clusters of gold particles, while other areas have no visible gold. Still, gold particles are abundant in large parts of the image. The gold particles seen in the image vary in size from 60 nm to a few nm. The majority of the particles are relatively small on this scale; most are smaller than 15 nm.

Figure 4.5 shows a SEM image from sample 3. Here gold particles are found in almost all of the image, with some areas being more densely populated. The largest particles have dimensions of around 100 nm. However most of the particles are smaller, with dimensions of 30 nm or less.

Some clear differences can be seen between the images from samples 1 and 3. There is clearly less gold on sample 1, which is consistent with the lower intensity ratio. The number of gold particles is also smaller for sample 1. When comparing the samples it is also clear that the typical particle is smaller for sample 1 than for sample 3.

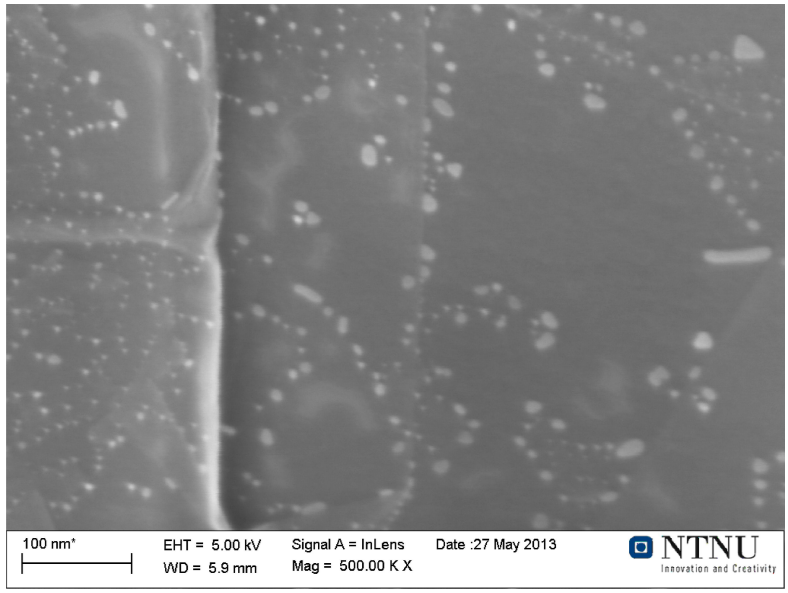

Figure 4.4: SEM image of sample 1. Gold particles can be seen as bright dots thinly distributed over most of the image. They are distributed somewhat unevenly, with clusters of particles in some areas and fewer particles in others. The particles range in size from 60 nm *to a few* nm *in diameter, with the majority being smaller than* 15 nm.

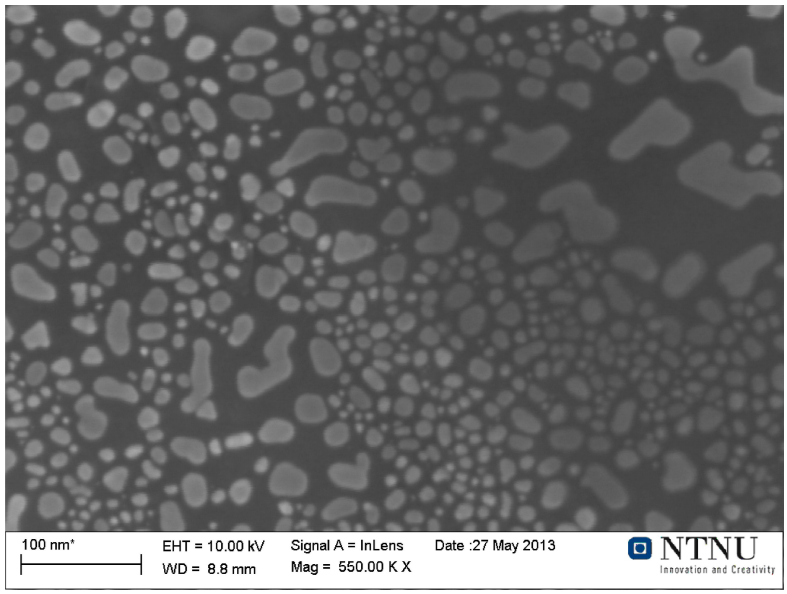

Figure 4.5: SEM image of sample 3. Gold particles can be seen as bright fields distributed over most of the image. There are some areas where there is little gold, but the number of gold particles is high over most of the image. The particles vary in size, with the largest particles having dimensions of up to around 100 nm. *Most of the particles are however smaller than about* 30 nm *in diameter.*

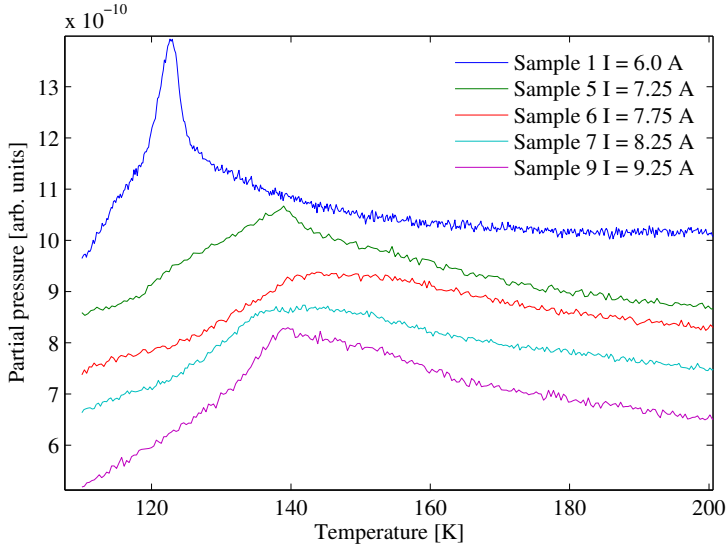

Figure 4.6: TPD spectra of samples 1, 5–7 and 9. The evaporation currents used when depositing gold on the samples are given in the legend, and can also be found in table 3.1. It should be noted that sample 1 was prepared before the gold source was replaced. Table 4.1 also shows that these samples have deposited about the same amount of gold on them, as indicated by similar intensity ratios of $I_{Au}/I_C = 0.0100 \pm 0.0012$. *The approximate temperature of the desorption peaks can also be found in table 4.1. The desorption peak of sample 1 is shifted to lower temperatures by about* 20 K *compared to the other samples shown here. There does not seem to be any systematic trend in the shift of the remaining samples. Also note that the sample 5 spectrum has a shoulder located around* 120 K. *This shoulder is not found in the spectra of samples 6, 7 and 9.*

4.3 The effect of changing the evaporation rate

Samples 1, 5–7 and 9 are used to examine the effect of varying the gold evaporation rate. All these samples have approximately the same amount of gold deposited, as indicated by the intensity ratios that are in the range $I_{Au}/I_C = 0.0100 \pm 0.0012$. Measured intensity ratios are listed in table 4.1. The evaporation rate is varied by changing the evaporation current and using the appropriate evaporation time to get the desired intensity ratio. Evaporation currents and times used can be seen in table 3.1. It should be noted that sample 1 was prepared prior to the replacement of the gold source, and might not be directly comparable to the samples prepared using the new source.

Figure 4.6 shows the TPD spectra from samples 1, 5–7 and 9. Even though the spectra were recorded up to 400 K, they have been truncated at 200 K because no features of interest are found above this temperature. Approximate positions of the desorption peaks can be found in table 4.1. The peak of the sample 1 spectrum is at 123 K, while all the other spectra have peaks around 140 K. All the shifts of the desorption peaks are relatively small, except the shift of around 20 K from sample 1 to the other samples. There does not seem to be any systematic trend in the small shifts seen for samples 5–7 and 9.

Some of the TPD spectra have additional features that should be mentioned. The sample 1 spectrum has a relatively sharp peak compared to the other spectra, which have peaks that are wider. In the spectrum from sample 5 we can also see a shoulder located around 120 K that is not found in the otherwise similar spectra from samples 6,7 and 9.

In figure 4.7 a SEM image of sample 6 is shown. Gold deposited on the sample can be seen as bright spots covering most of the imaged area. Although some areas have a higher density of gold particles than others, and some areas seem to have none, the particles are fairly evenly distributed. The gold particles mostly have a diameter of less than 20 nm, and many of them are smaller than 10 nm. In addition, the layered structure of graphite can be seen clearly in this image. Layers of the substrate are stacked and partially overlapping. Some of the edges are very regular,almost straight. Others are more irregular. How closely they are packed also varies, and there are large variations in the gaps between different layers.

Figure 4.8 shows a SEM image of sample 9. Roughly, two types of regions can be seen. One is characterized by a larger number of relatively small gold particles. These are for the most part smaller than 15 nm. In some areas these smaller particles are distributed in what seems like patterns, roughly in the shape of concentric semicircles. In the other type of region there are typically

fewer particles of larger sizes in the 15 nm to 30 nm range. These particles are also more spread out, with areas free from gold particles between them. While some of these larger particles have an irregular shape, a lot are shaped like equilateral triangles. These are of particular interest, as none of these are found in the images of sample 6. The bright diagonal seen across the lower left corner of the image is caused by a ledge or similar fault in the substrate material. The large and very bright irregular particle seen near the center of the image is presumed to be a contaminant, such as i.e. a grain of dust.

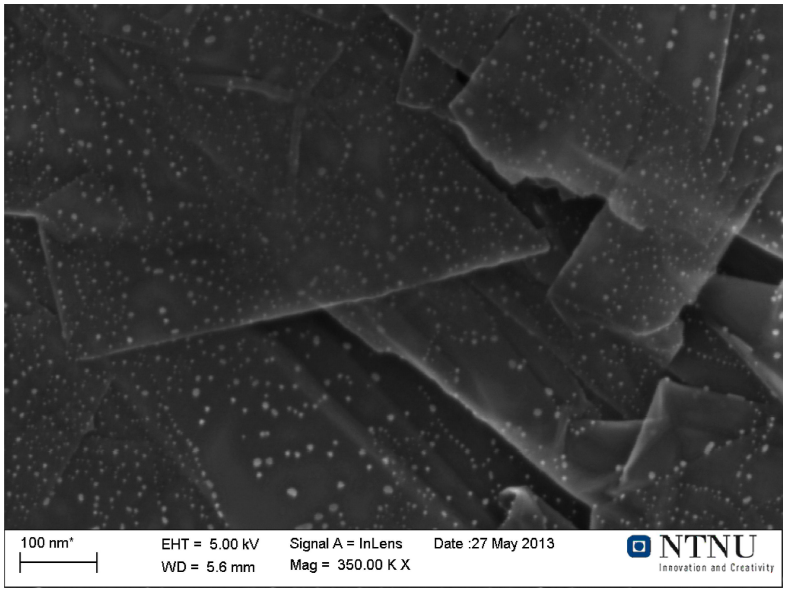

Figure 4.7: SEM image of sample 6. Gold particles can be seen as bright spots covering most of the substrate that is imaged. Layers that make up the structure of graphite can also be seen. The gold particles have a rounded shape and mostly have a diameter of less than 20 nm*, with a lot of them being smaller than* 10 nm*.*

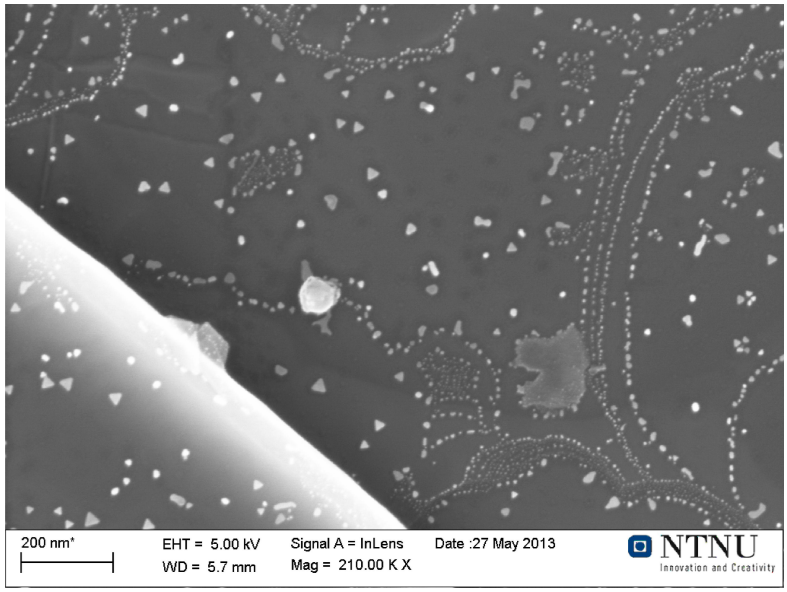

Figure 4.8: SEM image of sample 9. Gold particles can be seen as bright spots. Two types of regions are seen in this image. One has a high density of relatively small particles, of which some seem to form patterns. The particles here are for the most part smaller than 15 nm. *The other regions have fewer but relatively large particles. These mostly have dimensions of* 15 nm *to* 30 nm. *Some of these are shaped like equilateral triangles. In the lower left corner a ledge can be seen as a bright diagonal field. Near the center of the image what is presumed to be a contaminant can be seen.*

Chapter 5

Discussion

5.1 XPS measurements

There are two aspects of the XPS measurements that need to be discussed. They are the intensity ratios calculated, and the lack of systematic shifts in the core level binding energies.

The intensity ratio I_{Au}/I_C is calculated using eq. (2.2) and serve as a measurement of the amount of gold that is deposited on a given sample. Earlier studies of gold nanostructures on graphite have found much higher intensity ratios than those seen in table 4.1. This study has however found intensity ratios that are comparable to those found for very small platinum nanostructures [1,3].

XPS is a macroscopic technique that averages the signal over an area of several square millimetres. This means that samples with similar intensity ratios can be very different on a microscopic scale. Different areas on the same sample can also have very different characteristics.

The intensity ratios are calculated from the measured spectra using a MATLAB script that numerically integrates the photoemission peak. The limits of this integration is determined manually by visual inspection. This might lead to errors in the intensities calculated, in particular at lower intensities where the proper position of the limits are hard to determine due to low signal to noise ratio. In these experiments a higher number of iterations over the relevant energy range was used to increase the sensitivity when doing XPS measurements. Consistent choices for the limits of the numerical integration was used to minimize errors.

Shifts in the binding energy of the Au4f core level peak can be seen for some of the samples, as shown in table 4.1. However these do not follow any systematic trend, and most of them are relatively small. Earlier studies of platinum nanostructures on graphite have found a systematic shift in the core level binding energy associated with the effective size of the nanostructures [3]. This was attributed to a unit charge distributed over the nanostructure at the end of the photoemission process, as described by *Wertheim et. al.* [20]. From the SEM images of samples 1 and 3 in figures 4.4 and 4.5 it seems clear that there is an increase in the average size of the gold particles from sample 1 to 3. That no core level shift is observed could be because the XPS signal is averaged over the many types of gold particles on the graphite. This would hide the core level shift that would otherwise be seen for the smaller particles. Gold trapped at the edges of layers, grain boundaries and other imperfections will also play a part in this, as it will not have the same characteristics as the small gold particles.

5.2 The effect of changing intensity ratio

When comparing the SEM images of samples 1 and 3 seen in figures 4.4 and 4.5, obvoius differences are the number and the size of the particles. As graphite is a weakly interacting substrate, gold atoms impinging on the substrate will diffuse some distance before adhering to the surface. The first gold atoms in an area of clean substrate is most likely to adhere to a defect or impurity in the substrate. Further atoms are likely to adhere to the gold particles that already have nucleated, thus growing the particles [21]. It is therefore reasonable to assume that the differences in the number of gold particles in various areas of the same sample are related to variations in the number of nucleation sites, such as substrate defects and impurities. The generally higher number of particles in sample 3 can possibly be an effect of a higher number of nucleation sites, but as all the samples were prepared in the same way, it is more likely that it is an effect of the larger amount of gold evaporated on to the sample. There has simply been more opportunities for gold particles to nucleate. The increases in the general size of the particle is then also explained by the larger amount of gold, as there has been more gold available to grow the particles. Increased particle size with higher intensity ratios is consistent with earlier studies of platinum nanostructures on graphite [1].

Julukian et. al. [3] examined the effect of size on the TPD spectrum of CO from platinum nanostructures. It was found that smaller structures led to a shift

in the TPD spectrum towards lower temperatures. The SEM images of samples 1 and 3 clearly show that the gold structures are larger on sample 3. The shift in the spectra from samples 1–3 seen in figure 4.3 can therefore possibly be explained as a size effect.

These spectra are also distinguished by distinctive features that mark them. While sample 1 and 3 have sharp distinct peaks, sample 2 has a more blunted and broad peak like those found for samples 5–7 and 9. In addition, sample 3 has a small second peak. One possible explanation for this is experimental discrepancies. It could in theory be caused by changes in the heating rates used when recording the spectra. The heating of the samples were recorded and checked to see that they were smooth and that the heating rate (table 3.1) was consistent between samples, but these are still factors that are hard to control completely in the experimental set-up used. Effects from the different sample holders that were used, and also their removal from the vacuum chamber between each measurement, could also affect the TPD spectra.

Another possible explanation is that the broad peak found for sample 2 is the result of the combination of more than one separate peak that can not be distinguished, but is seen as one broader peak. Both computer simulations and experiments have previously shown that desorption peaks broaden at higher adsorbate coverages when there are more adsorption sites used and more adsorbate-adsorbate interaction [13, 22, 23]. The samples examined here are complex, with many possibilities for adsorption sites and interaction between adsorbate and substrate. This could in theory give rise to adsorption peaks at different temperatures and to broadening of the peaks. In addition to adsorption in connection with the cold particles and on the gold-free graphite areas, it is also possible that CO is adsorbed within the graphite due to its layered structure. Such layers can clearly be seen in figure 4.7. As TPD is a macroscopic technique, the signal will be averaged over an area of some square millimetres. The sample is not uniform, and the contribution from areas with differing properties can also be a factor in broadening of the desorption peak. Comparison with the desorption spectrum of clean graphite could give insights into what effects are from the substrate, and what effects that are dependent on the deposited gold.

If the broad peak seen for sample 2 is comprised of several peaks that can not be distinguished, the more distinctive peaks seen for sample 1 and 3 might be the result of one or more of these peaks showing up more clearly. Why this happens is not clear. It could possibly be caused by the change in the size and number of gold particles. There are also some distinct features that are seen around the same temperature of 120 K in several spectra. These are the main

peak from sample 1, the small second peak fro sample 3 and the shoulders seen on the rising edge from samples 2 and 5. It is possible that these are related to the same adsorption phenomenon as they are found at approximately the same temperature.

5.3 The effect of evaporation rate

That there is no trend to the small shifts seen in the TPD spectra for samples 5–7 and 9 in figure 4.6 indicates that the evaporation rate does not influence the adsorption properties of the samples in the region that has been examined. Sample 1 has the same intensity ratio I_{Au}/I_C as samples 5–7 and 9, but its TPD spectrum is shifted to a lower temperature. The reason for this is not known, but it should be noted that sample 1 was prepared before the gold source was replaced, and might not be directly comparable to the samples prepared using the new source.

When comparing the SEM images of sample 6 and sample 9 seen in figures 4.7 and 4.8 the most striking difference is the emergence of a larger number of triangular gold particles on sample 9. The amount of gold on these two samples are more or less the same, as shown by the intensity ratios. It is therefore reasonable that the larger number of triangular gold particles is an effect of the change in evaporation rate.

That gold deposited on graphite can form dendritic nanostructures is well known. Their characteristics and growth has been the subject of multiple studies [21, 24–26]. The appearance of anisotropic structures is therefore not surprising. *Julukian et. al.* [1] studied dendritic nanostructures of platinum on graphite, and found that the particles changed between different forms depending on the amount of platinum deposited. In the same way, the triangular particles seen on sample 9 might represent an early stage of evolution of gold nanostructures in the regime where diffusion dominates the particle formation. *Julukian et. al.* [1] also pointed out that studies of similar systems using various materials have found that the characteristics of nanostructures can depend on factors such as temperature, particle size, particle flux and substrate roughness.

Scott et. al. [2] found that the growth of nanostructures of antimony on graphite is dependent on the particle flux during deposition. They suggest a mechanism where new particles captured by the structures does not have time to relax to a more thermodynamically advantageous configuration before being fixed in position by a new particle arriving. A similar effect might cause higher number of triangular particles seen on sample 9. The balance between

thermodynamic effects that favour more isotropic particles and the kinetics that favour anisotropic particles is changed when the particle flux is increased. The gold triangles found here are however very small compared to those structures studied in [2], but in the same size range as the smaller of the structures studied in [1].

Chapter 6

Conclusion

6.1 Concluding remarks

The intensity ratios measured for the gold deposited on graphite substrates are significantly lower than those found in previous studies [4]. Earlier studies on platinum have shown that the intensity ratio is correlated with the size of the metal particles on the surface [1]. This was also found in the samples studied here, and can clearly be seen in the SEM images. No significant trend in the core level shifts were observed in the XPS spectra for particles of different sizes, in contrast to what has previously been found for platinum [3]. A possible cause for this can be influence from substrate imperfections.

A trend in the shift of the TPD spectra is seen for the samples where the intensity ratio is varied. This could be caused by the change in gold particle size, as have previously been found for platinum [3]. Variations in the appearance of the TPD spectra might also be caused by complicated adsorption/desorption mechanisms, substrate effects or inconsistencies with the heating and the sample holders.

The TPD data shows no clear trend when the evaporation rate is varied while approximately the same intensity ratio is maintained. At lower evaporation rates the gold nanoparticles are mostly isotropic aggregates. Anisotropic triangular particles appear at the highest evaporation rate. These might be an early stage of the growth of more complex gold nanostructures in the regime where diffusion dominates the particle formation [1].

6.2 Further work

More research is needed to confirm the trend seen in the TPD data for variations of the intensity ratio. Studying samples with a wider range of intensity ratios would more clearly show such a trend. Varying amounts of gold can be deposited at relatively high evaporation rates. This can be used to study the evolution of gold nanostructures in the regime where diffusion effects dominate their growth patterns. Another approach is to use ion beam sputtering to remove material from nanostructures, as opposed to adding material by evaporation. Using this method, size effects can be studied on a single sample. This would help avoid problems caused by having to change both sample and sample holders between experiments.

Bibliography

[1] A. Julukian, S. Raaen, and D. Franke, "Formation of Pt nanostructures on graphite and transition from nano-spiders to nano-flakes," unpublished.

[2] S. A. Scott and S. A. Brown, "Three-dimensional growth characteristics of antimony aggregates on graphite," *Eur. Phys.J. D*, vol. 39, no. 3, 2006. [Online]. Available: http://dx.doi.org/10.1140/epjd/e2006-00123-2

[3] A. Julukian, T. Fadnes, S. Raaen, and M. Balci, "Size effect on thermal desorption of CO from Pt nanostructures on graphite," *J. Appl. Phys.*, vol. 109, no. 12, 2011. [Online]. Available: http://link.aip.org/link/?JAP/109/123503/1

[4] T. K. Karlsen, "Gold and Platinum Surface Nanostructures on Highly Oriented Pyrolytic Graphite," Master's thesis, Norwegian University of Technology and Science, 2012.

[5] C. R. Brundle, C. A. J. Evans, and S. Wilson, Eds., *Encyclopedia of Materials Characterization - Surfaces, Interfaces, Thin Films*. Elsevier, 1992.

[6] B. Bransden and C. Joachain, *Quantum mechanics*, 2nd ed. Pearson/Prentice Hall, 2000.

[7] S. Raaen, "Lecture notes on Electron Spectroscopy," Institutt for fysikk, NTNU.

[8] R. L. Park and M. G. Lagally, *Solid state physics : Surfaces*, ser. Methods of experimental physics. Academic Press, 1985, vol. 22.

[9] D. P. Woodruff and T. A. Delchar, *Modern Techniques of Surface Science*. Cambridge University Press, 1994. [Online]. Available: http://dx.doi.org/10.1017/CBO9780511623172

[10] A. Zangwill, *Physics at Surfaces*. Cambridge University Press, 1988.

[11] Webpage of the Alberta Centre for Surface Engineering and Science. [Online]. Available: http://www.ualberta.ca/ACSES/ACSES3/Techniques/XPS/xps_xee.htm

[12] B. V. Crist, *Handbook of Monochromatic XPS Spectra - The Elements and Native Oxides*. John Wiley & Sons, 2000.

[13] S. Raaen and A. Ramstad, "Monte-Carlo simulations of thermal desorption of adsorbed molecules from metal surfaces," *Energy*, vol. 30, no. 6, 2005. [Online]. Available: http://www.sciencedirect.com/science/article/pii/S0360544204001872

[14] S. E. Van Bramer, "An Introduction to Mass Spectrometry," 1997. [Online]. Available: http://science.widener.edu/svb/massspec/massspec.pdf

[15] K. Mills and J. R. Davis, *ASM Handbook, Volume 12 - Fractography*. ASM International, 1987. [Online]. Available: http://www.knovel.com/web/portal/browse/display?_EXT_KNOVEL_DISPLAY_bookid=3116&VerticalID=0

[16] M. Dunlap and J. E. Adaskaveg, "Introduction to the Scanning Electron Microscope. Theory, Practice, & Procedures," 1997. [Online]. Available: https://imf.ucmerced.edu/downloads/semmanual.pdf

[17] Wikipedia: Scanning Electron Microscope. [Online]. Available: http://en.wikipedia.org/wiki/Scanning_electron_microscope

[18] J. H. Moore, C. C. Davis, M. A. Coplan, and S. C. Greer, *Building Scientific Apparatus*, 4th ed. Cambridge University Pressr, 2009.

[19] E. Espeland, "Self-assembeled gold nanostructures on a graphite substrate," Project report, Institutt for fysikk, NTNU.

[20] G. K. Wertheim, S. B. DiCenzo, and S. E. Youngquist, "Unit Charge on Supported Gold Clusters in Photoemission Final State," *Phys. Rev. Lett.*, vol. 51, 1983. [Online]. Available: http://link.aps.org/doi/10.1103/PhysRevLett.51.2310

[21] T. Darby and C. Wayman, "Nucleation and growth of gold films on graphite: I. Effects of substrate condition and evaporation rate," *J. Cryst. Growth*, vol. 28, no. 1, 1975. [Online]. Available: http://www.sciencedirect.com/science/article/pii/0022024875900251

[22] A. Ramstad and S. Raaen, "Formation of and CO adsorption on an inert La-Pt(111) surface alloy," *Phys. Rev. B*, vol. 59, Jun 1999. [Online]. Available: http://link.aps.org/doi/10.1103/PhysRevB.59.15935

[23] M. Juel and S. Raaen, "Thermal desorption of carbon monoxide from Mo(110)," *Philosophical Magazine*, vol. 83, no. 21, 2003. [Online]. Available: http://www.tandfonline.com/doi/abs/10.1080/1478643031000116023

[24] C. Wayman and T. Darby, "Nucleation and growth of gold films on graphite: II. The effect of substrate temperature," *J. Cryst. Growth*, vol. 28, no. 1, 1975. [Online]. Available: http://www.sciencedirect.com/science/article/pii/0022024875900263

[25] T. Darby and C. Wayman, "Growth of gold thin film dendrites on graphite substrates," *J. Cryst. Growth*, vol. 29, no. 1, 1975. [Online]. Available: http://www.sciencedirect.com/science/article/pii/0022024875900561

[26] R. Anton and I. Schneidereit, "*In situ* TEM investigations of dendritic growth of Au particles on HOPG," *Phys. Rev. B*, vol. 58, Nov 1998. [Online]. Available: http://link.aps.org/doi/10.1103/PhysRevB.58.13874

List of Figures

List of Tables